J. Fluid Mech. (2012), *vol.* 705, *pp.* 258–279. © Cambridge University Press 2011
doi:10.1017/jfm.2011.438

Steady motion of Bingham liquid plugs in two-dimensional channels

Parsa Zamankhan[1]†, Brian T. Helenbrook[2], Shuichi Takayama[1] and James B. Grotberg[1]

[1] Department of Biomedical Engineering, University of Michigan, Ann Arbor, MI 48109, USA

[2] Department of Mechanical and Aeronautical Engineering, Clarkson University, Potsdam, NY 13699, USA

(Received 7 May 2011; revised 19 September 2011; accepted 3 October 2011; first published online 12 December 2011)

We study numerically the steady creeping motion of Bingham liquid plugs in two-dimensional channels as a model of mucus behaviour during airway reopening in pulmonary airways. In addition to flow analysis related to propagation of the plug, the stress distribution on the wall is studied for better understanding of potential airway epithelial cell injury mechanisms. The yield stress behaviour of the fluid was implemented through a regularized constitutive equation. The capillary number, *Ca*, and the Bingham number, *Bn*, which is the ratio of the yield stress to a characteristic viscous stress, varied over the ranges 0.025–0.1 and 0–1.5, respectively. For the range of parameters studied, it was found that, while the yield stress reduces the magnitude of the shearing along the wall, it can magnify the amplitude of the wall shear stress gradient significantly, and also it can elevate the magnitude of the wall shear stress and wall pressure gradient up to 30 % and 15 %, respectively. Therefore, the motion of mucus plugs can be more damaging to the airway epithelial cells due to the yield stress properties of mucus. The yield stress also modifies the profile of the plug where the amplitude of the capillary waves at the leading meniscus decreases with increase in *Bn*. Other findings are that: the thickness of the static film increases with increasing *Bn*; the driving pressure difference increases linearly with *Bn*; and increasing *Bn* extends any wall stagnation point beneath the leading meniscus to an unyielded line segment beneath the leading meniscus. With an increase in *Bn*, the unyielded areas appear and grow in the adjacent wall film as well as the core region of the plug between the two menisci. The plug length, L_P, mostly modifies the topology of the yield surfaces. It was found that the unyielded area in the core region between the two menisci grows as the plug length decreases. The very short Bingham plug behaves like a solid lamella. In all computed liquid plugs moving steadily, the von Mises stress attains its maximum value near the interface of the leading meniscus in the transition region. For Bingham plugs moving very slowly, $Ca \rightarrow 0$, the driving pressure is non-zero.

Key words: liquid bridges, plastic materials, pulmonary fluid mechanics

---

† Email address for correspondence: parsa@umich.edu

https://doi.org/10.1017/jfm.2011.438 Published online by Cambridge University Press

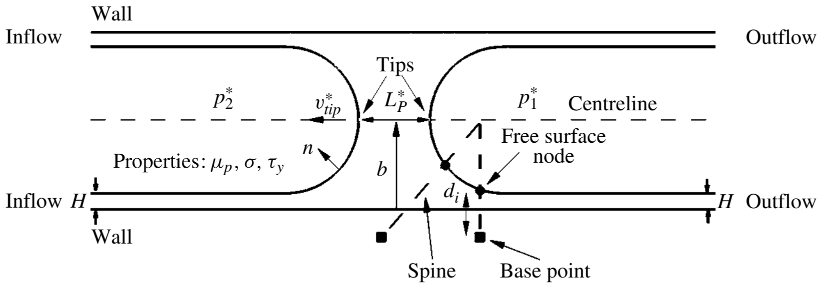

FIGURE 1. A schematic from the domain of calculation for the steady motion of a liquid plug in a two-dimensional channel.

1. Introduction

Liquid plugs can be formed in airways through the introduction of liquids into liquid-lined conduits, accumulation due to cough or gravity-driven drainage, or Rayleigh instability of the coating liquids in such conduits (Burger & Macklem 1968; Everett & Haynes 1972; Kamm & Schroter 1989; Halpern & Grotberg 1992; Bian *et al.* 2010; Tai *et al.* 2011). In addition, the spaces between consecutive gas bubbles in Taylor flow (Shao, Gavriilidis & Angeli 2009) are filled by liquid plugs. Liquid plugs are formed in the lung under a variety of circumstances, including disease states that cause an excess of liquid there, or reductions of surfactant activity, which increases the surface tension. As a result, they block the gas exchange in some sections of the lung. Understanding the mechanisms involved in the formation of mucus plugs in the respiratory airways, however, requires a separate study. The blocked airways can be reopened through introducing a critical driving pressure difference across the plug. The reopening procedure, however, can cause the injury of epithelial cells that cover the surface of the airway. Plug propagation due to the pressure difference induces stresses and stress gradients along the wall, which can lead to lethal damage of the epithelial cells (Huh *et al.* 2007; Tavana *et al.* 2011). For Newtonian plugs with capillary number $Ca < 0.05$, the most damaging feature is the leading meniscus region where a capillary wave extends ahead and creates the thinnest film location with the highest stresses and stress gradients. The distribution of the boluses of liquid drugs during surfactant replacement therapy (SRT) (Long *et al.* 1991; Halpern, Jensen & Grotberg 1998; Espinosa & Kamm 1999; Waters & Grotberg 2002) also involves propagation of the liquid plugs in the airway conduits.

Figure 1 shows a scheme of a liquid plug. It contains the fluid region between a forward and backward gas finger confined by solid walls. The plug length is the distance between the two menisci tips. While the leading and trailing menisci in a liquid plug may represent the rear and front sections of a long bubble, the analysis of a liquid plug is more general than a single long bubble, since in short plugs the two menisci interact during the motion. In addition, the driving pressure difference between the two menisci cannot be determined through studying any individual gas bubble.

Howell, Waters & Grotberg (2000), through an analytical study identified the critical driving pressure for reopening of a flexible tube blocked by a Newtonian plug. They showed that, for a given precursor film thickness, the critical driving pressure decreases with decreasing hoop and longitudinal tube tension.

Fujioka & Grotberg (2004) studied numerically the steady motion of liquid plugs consisting of Newtonian fluids in two-dimensional channels. The effects of fluid inertia, viscous stresses and surface tension were examined in terms of three

https://doi.org/10.1017/jfm.2011.438 Published online by Cambridge University Press

dimensionless numbers: capillary number, Ca, dimensionless plug length, L_P, and Reynolds number, Re. Their results show that the shape of the two menisci is affected significantly by Ca and Re. For small and moderate Ca, capillary waves were observed along the leading meniscus. The amplitude of the waves was shown to increase with increasing Re or decreasing Ca. The results also show that the interaction between the two menisci becomes significant when the dimensional length of the plug is less than half the width of the channel and the fluid inertia is involved. The study also presents the required driving pressure in term of Ca, Re and L_P for steady motions.

Later Fujioka & Grotberg (2005), Zheng, Fujioka & Grotberg (2007) and Zheng *et al.* (2009) included the effects of the gravity, surfactant and flexible walls into their model for the steady motion. It turned out that each of those factors affects the menisci shapes and the wall stresses significantly. The presence of the surfactant (Fujioka & Grotberg 2005; Zheng *et al.* 2007) increases the minimum of the film thickness and as a result it reduces the maximum wall shear stress. When gravity is perpendicular to the wall (Zheng *et al.* 2007), it shifts the plug tips to a position above the midline and as a result the plug becomes asymmetric with respect to the channel centreline. The upper and lower halves interact by a fluid flow originating from the upper trailing film, passing through the core region between two menisci and then entering into the lower trailing film. The stresses are larger on the upper wall and their amplitudes increase with increasing Bond, Bo, and Reynolds, Re, numbers. The computational results of Zheng *et al.* (2009) show that the stress levels and their gradients on the highly deformable walls are larger than those on the solid walls. This suggests that, in diseases such as emphysema where the airway walls are more deformable, the chance of epithelial cell injuries by the plug motion is higher.

Fujioka, Takayama & Grotberg (2008) also studied the transient propagation of a liquid plug under a constant dimensionless driving pressure, $\Delta\pi$, in a liquid-coated tube. The study showed that, depending on the values of the dimensionless parameters, for $\Delta\pi$ larger than a critical value the plug length decreases during the motion and it eventually ruptures. For $\Delta\pi$ lower than the critical value, however, the plug length increases as it propagates and as a result it does not rupture.

In all previous work the plugs consist of Newtonian fluids. The inner side of the respiratory airways, however, is covered by a non-Newtonian mucus layer, which rests on a Newtonian serous layer. Mucus has a yield stress, one of its important non-Newtonian properties. The liquid plugs in the airway that develop through the closure mechanism, therefore, consist of non-Newtonian fluids with a yield stress. This would lead to some major differences compared to Newtonian plugs during propagation.

Non-Newtonian fluids with a yield stress, τ_y, behave like solids below the yield stress, while above it they behave like fluids. A few examples out of many are: blood and mucus as biological fluids; ketchup and mayonnaise as food products; gels, pastes and paints as goods in daily life; and nuclear waste suspensions as fluids arising from a series of industrial processes. The macroscopic behaviour of the yield stress fluids can be analysed with some accuracy via some proposed constitutive equations. Among them, the simplest one is the constitutive equation for a Bingham fluid, i.e. the Bingham equation. It assumes a linear relation between the viscous stress and the rate-of-strain tensors for von Mises stresses above τ_y, while for von Mises stresses below τ_y it assumes that the material behaves like a solid. Depending on the local value of the stresses, this divides the material domain into the yielded and unyielded regions with liquid- and solid-like behaviours, respectively. The Bingham equation introduces a new dimensionless parameter, the Bingham number, Bn, which is an indicator of the ratio of τ_y to a characteristic viscous stress. Herschel–Bulkley (Beaulne & Mitsoulis

https://doi.org/10.1017/jfm.2011.438 Published online by Cambridge University Press

1997) and Casson (Fung 1984) are two other major constitutive equations for yield stress fluids in which the stress–strain rate relationship above τ_y is not linear. In most circumstances they represent the behaviour of the yield stress fluids in a better way. However, they make the numerical simulations harder to perform.

To the best of our knowledge, there is no published work about the propagation of Bingham plugs in conduits in the open literature. However, some investigators have studied problems with some level of similarities in the past. We review some of them in the following.

Dubash & Frigaard (2004), Potapov *et al.* (2006), Singh & Denn (2008), Tsamopoulos *et al.* (2008) and Lavrenteva, Holenberg & Nir (2009) through different approaches studied the rise of bubbles/drops in large containers filled by quiescent viscoplastic fluids. They all found a critical τ_y below which buoyancy causes flow. Lavrenteva *et al.* (2009) experimentally and Singh & Denn (2008) numerically showed that the presence of a second bubble/drop within a critical distance extends the yielded regions and eases the motion.

Dimakopoulos & Tsamopoulos (2003, 2007) numerically studied the transient displacement of an advancing gas finger into a constricted tube and a tube with an expansion at the inlet and a contraction at the outlet, filled by a Bingham fluid. They showed that, similar to the Newtonian fluids, a layer of the fluid is deposited on the wall as the finger advances through the tube. The thickness of the layer was shown to be a function of *Ca*, *Bn* and *Re*. They also discussed the variation of the finger shape, the location of the yield surfaces and the flow patterns.

Allouche, Frigaard & Sona (2000) studied a Bingham fluid finger propagating into a vertical channel filled with a second Bingham fluid that is displaced. They restricted their analytical and numerical investigations to creeping motion and negligible surface tension. Interestingly, they found a range of parameter values where the finger leaves a zero-thickness trailing film. Outside of this parameter range they predicted an upper bound for the thickness of the trailing film for each set of parameters.

De Sousa *et al.* (2007) and Thompson, Soares & Bacchi (2010) studied numerically the steady creeping motion of an advancing gas finger in a tube filled by power-law or Bingham fluids. They demonstrated that the flow regime and the topology of the yielded and unyielded regions are affected significantly by the dimensionless yield stress. For some range of the dimensionless yield stress, the computed yield surfaces were in contradiction with the Bingham fluid equation. They attributed this to the use of small regularized parameters in their simulations. Their results indicate that, as the gas finger advances, similar to the Newtonian fluids, a static liquid layer is formed adjacent to the wall. It can be inferred from their results that the thickness of the static layer increases with dimensional yield stress in some range.

All the aforementioned works dealing with an advancing finger resemble the trailing meniscus and not the leading one in a liquid plug. In the bubble-related works, the container is much larger than the bubble, so that the interaction between the bubble and the walls is negligible. In addition, the background flow is stationary. Therefore, to analyse the displacement of liquid plugs in conduits, some separate studies are required. It is worth noting that the simulations of the propagation of the liquid plugs are more challenging compared to those for advancing gas fingers owing to the presence of the leading meniscus in the plugs.

For the particular case of respiratory airways, they are lined with a serous–mucus bilayer. The serous layer is adjacent to the epithelial cells, and the mucus layer is next to the air core. Mucus has a yield stress under normal health conditions of 400–600 dyne cm^{-2}, though it can become much higher in diseases such as

https://doi.org/10.1017/jfm.2011.438 Published online by Cambridge University Press

asthma, emphysema and cystic fibrosis. When the plug forms, it can pull the flexible airway into a flattened elliptical cross-section (Heil 1999*a*,*b*) with an aspect ratio up to 20. Because of this geometry, a two-dimensional model is a representative of the reopening process of the occluded airways.

In this study the steady creeping motion of a liquid plug in a two-dimensional channel filled by a Bingham fluid is investigated numerically. (The current computations can be repeated for axisymmetric tubes without any difficulties.) This allows us to focus on the effects of non-Newtonian properties, which can later be compared to a fully bilayer system undertaking a transient motion. In the absence of fluid inertia and gravity, Bn, Ca and L_P are the input parameters, while the velocity and pressure field – and from them the fluid stresses on the wall – are to be computed. This provides the required driving pressure for the steady motion as well. Particular attention is given to the distribution of the stresses and their gradients along the wall and their modification by the yield stress for better understanding of the epithelial cell injury mechanisms in the respiratory airways.

2. Regularized constitutive equation

In the Bingham constitutive equation, the fluid tolerates any level of stress less than a threshold, the yield stress, without any strain rate. (The elastic deformation below the yield stress is neglected in this study.) Above the yield stress, it behaves as a generalized Newtonian fluid. The constitutive equation was formulated by Oldroyd (1947*a*,*b*) as

$$\begin{cases} \boldsymbol{\tau}^* = \left(\mu_p + \dfrac{\tau_y}{\dot{\gamma}^*}\right)\boldsymbol{D}^*, & \text{if } |\tau^*| > \tau_y, \\ \boldsymbol{D}^* = 0, & \text{if } |\tau^*| \leqslant \tau_y. \end{cases} \tag{2.1}$$

In (2.1), $\boldsymbol{\tau}^*$ is the viscous stress tensor, $\boldsymbol{D}^*$ is the rate-of-strain tensor, μ_p is the plastic viscosity, τ_y is the yield stress, $\dot{\gamma}^* = \sqrt{(1/2)D^*_{ij}D^*_{ij}}$ is the strain rate, and $|\tau^*| = \sqrt{(1/2)\tau^*_{ij}\tau^*_{ij}}$ is the von Mises stress.

In the Bingham equation, the transition from a rigid solid to a viscous liquid on a surface that is not known *a priori* produces significant difficulties in numerical simulations. Therefore, computational studies commonly use regularized constitutive equations instead of the Bingham equation to ease the difficulties (Allouche *et al.* 2000; Liu, Muller & Denn 2002; Dimakopoulos & Tsamopoulos 2003, 2007; de Sousa *et al.* 2007; Singh & Denn 2008). The regularized equations are continuous and are characterized by a regularization parameter. In this study we use a regularized method suggested by Papanastasiou (1987) through the following equations:

$$\boldsymbol{\tau}^* = \eta^* \boldsymbol{D}^*, \tag{2.2}$$

$$\eta^* = \mu_p + \frac{\tau_y}{\dot{\gamma}^*}(1 - \exp(-m^*\dot{\gamma}^*)), \tag{2.3}$$

where η^* is the apparent viscosity and m^* is the regularization parameter. For large enough values of m^*, the regularized method resemble the Bingham equation. Regularized equations are easier for programming. In addition, the obtained velocity fields and free surface profiles from them converge with m^*. However, in general, there is no guarantee for the convergence of the boundaries between the yielded and the unyielded regions, i.e. the yield surfaces with m^*, for the regularized methods (Burgos, Alexandrou & Entov 1999; Liu *et al.* 2002). In addition, as m^* increases, the

https://doi.org/10.1017/jfm.2011.438 Published online by Cambridge University Press

determination of the location of the yield surfaces become more sensitive to numerical errors.

The yield criterion for the regularized method is given by the following relation:

$$\begin{aligned} |\tau^*| \leqslant \tau_y, &\quad \text{unyielded}, \\ |\tau^*| > \tau_y, &\quad \text{yielded}. \end{aligned} \tag{2.4}$$

The criterion is used to determine the yield surfaces.

The augmented Lagrangian method (Glowinski, Lions & Tremolieres 1981; Glowinski 1984) is another approach to deal with the Bingham equation. Some investigators (Vola, Boscardin & Latche 2003; Moyers-Gonzalez & Frigaard 2004; Vola, Babik & Latche 2004; Zhang 2011) have used it for Bingham fluids recently and resolved the yield surfaces more accurately compared to the regularized methods. To the best of our knowledge, however, the method has not yet been implemented for free surface problems of Bingham fluids with surface tension effects.

3. The governing equations and boundary conditions

Figure 1 shows a schematic of the domain of calculation for a liquid plug with a length of L_P^* including a leading and a trailing meniscus on the left and right, respectively. Each meniscus includes a transition region where the distance between the interface and the wall varies with x and a flat one where the distance is constant. The plug under a constant driving pressure difference, $\Delta p^* = p_1^* - p_2^*$, is moving from the right to the left with a constant speed, v_{tip}^*, in a two-dimensional channel filled by a Bingham fluid. Neglecting the gravitational force, only the lower half of the domain is adequate for the analysis. To work with the steady form of the governing equations, the frame of reference is attached to the tip of the plug. Owing to the small values of the gas–liquid density and viscosity ratios, the effects of gas phase on the motion of the liquid phase are negligible. Therefore, the conservation equations are not solved for the gas phase. The effects of surfactants in liquid plugs on the liquid–gas surface tension were neglected. As a result, the shear stress along the gas–liquid interfaces is zero. The velocity components are scaled by v_{tip}^*; the length dimensions by the half-width of the channel, b; the pressure and stresses by $\mu_p v_{tip}^*/b$; the strain rate by v_{tip}^*/b; and the regularization parameter by b/v_{tip}^*.

Then the dimensionless forms of the governing equations for the liquid phase with constant properties are given by: continuity

$$\nabla \cdot \boldsymbol{V} = 0, \tag{3.1}$$

cauchy momentum

$$-\nabla p + \nabla \cdot \boldsymbol{\tau} = 0, \tag{3.2}$$

where the viscous stress tensor is calculated via Papanastasiou's regularized equations (Papanastasiou 1987), given by

$$\boldsymbol{\tau} = \eta \boldsymbol{D}, \tag{3.3}$$

$$\eta = 1 + \frac{Bn}{\dot{\gamma}}(1 - \exp(-m\dot{\gamma})). \tag{3.4}$$

In the above equations, p is the pressure and $Bn = \tau_y b/\mu_p v_{tip}^*$ is the Bingham number, which represents the ratio of the yield stress to a characteristic viscous stress.

The boundary conditions along the plug surface are: kinematic

$$\boldsymbol{V} \cdot \boldsymbol{n} = 0, \tag{3.5}$$

https://doi.org/10.1017/jfm.2011.438 Published online by Cambridge University Press

stress

$$-p\boldsymbol{n} + \eta(\nabla \boldsymbol{V} + (\nabla \boldsymbol{V})^{\mathrm{T}}) \cdot \boldsymbol{n} = \frac{\kappa}{Ca}\boldsymbol{n} - p_i\boldsymbol{n} \quad (i = 1, 2), \tag{3.6}$$

where $\boldsymbol{n}$ is the normal unit vector, κ is the local curvature and $Ca = \mu_p v^*_{tip}/\sigma$ is the capillary number, which represents the ratio of a characteristic viscous stress to the surface tension. The subscripts 1 and 2 stand for the gas phases adjacent to the leading and trailing menisci, respectively.

At the wall, the inflow and outflow velocity components in the moving frame of reference are

$$V_x = 1, \tag{3.7}$$

$$V_y = 0. \tag{3.8}$$

In the steady motion, the plug length, L_P, remains constant and the two menisci intersect the plane of symmetry with a right angle.

Ca, Bn and L_P are the input parameters, while the profile of the two menisci along with the velocity and pressure fields including Δp are to be computed. In most of the simulations, m is 1000. We analyse the effects of the value of m on the results as well.

4. Numerical procedure

For numerical simulations a commercial package, ANSYS FIDAP, is used. The governing equations are discretized with a finite element mixed-discontinuous standard Galerkin formulation. In the utilized elements, $\boldsymbol{V}$ and p are interpolated with quadratic and linear interpolation functions, respectively.

To resolve the free surface, we used the method of spines developed by Kistler & Scriven (1984). In this method, the displacement of the computational nodes on the free surface is restricted to be along some predefined lines, spines. The location of each node on the free surfaces is then parametrized through its distance, d_i, from a specific point along the spine, a base point. Velocity components and pressure for all the nodes in the domain along with d_i for the nodes on the free surfaces are the unknowns of the discretized system of equations and their boundary conditions, (3.1)–(3.8). The values of d_i determine the shape of the free surfaces. To maintain the quality of the mesh, the nodes beneath the free surfaces are also allowed to move along the spines proportional to the displacement of the nodes on the free surfaces. In some circumstances, choosing suitable directions for the spines is crucial so that convergence is achieved. The final shape of the free surfaces, however, is independent of the directions of the spines. Figure 1 shows a scheme from the computational nodes on the free surfaces, spines and the base points. The resulting nonlinear system of equations is solved by the quasi-Newton method. The inverse of the sparse Jacobian matrix is computed by a skyline Gaussian elimination method.

All the nodes along the two interfaces, including the two end points and the two tips, are allowed to move along the predefined spines. Bn and Ca are the input parameters and Δp is iteratively adjusted so that the desired L_P is obtained. There is no extra condition to relate the displacement of the two end nodes. For the converged solutions, however, the film thickness at the two ends turns out to be the same to machine precision. This further demonstrates that the converged solutions satisfy the conservation of mass to machine precision since V_x is set to 1 at the two ends by (3.7).

The inflow and outflow boundaries were put far enough from the two tips that their locations do not affect the results. For the computed cases, it was observed that a

https://doi.org/10.1017/jfm.2011.438 Published online by Cambridge University Press

distance of four times the channel width between the tips and the end boundaries is adequate for this purpose.

The computational grid consists of ∼15 000–18 000 elements and 60 000–70 000 nodes depending on the values of the dimensionless parameters. The CPU time on average for each case on a 2.53 GHz personal computer is ∼10 min. To achieve the convergence through the quasi-Newton method, the simulations were done in sequences with gradual variation in the dimensionless parameters. More specifically, the solution for each case was used as an initial condition for the next. As Bn became larger and L_P became shorter, the dimensionless parameters were changed more slightly from one case to the next so that convergence is achieved. Under circumstances where the grids are highly distorted, the domain that includes the correct shape of the interfaces was re-meshed manually and then computations were repeated. We have not observed any recognizable differences between the shape of the interfaces after and before the re-meshing. The regularized constitutive equation is introduced through an ANSYS FIDAP user subroutine. More information regarding the problem setup can be found in the user manual (ANSYS FIDAP 2003).

5. Range of the dimensionless parameters

For a steady motion, the dimensionless numbers, Bn and Ca, and Re in different generations of the respiratory airways can be represented by the following relations:

$$Bn(n) = \tau_y \pi d_0^3/\mu_p Q, \tag{5.1}$$

$$Ca(n) = 4\mu_p Q/\pi 2^{n/3} d_0^2 \sigma, \tag{5.2}$$

$$Re(n) = 4\rho Q/2^{2n/3}\pi \mu_p d_0. \tag{5.3}$$

In the above relations, n is the generation number, d_0 is the diameter of the trachea, and Q is the average breathing rate. In deriving the above relations, it was assumed that the anatomy of the respiratory airways is determined by the Weibel model (Weibel 1963) through $d_n = d_0 2^{-n/3}$, where d_n is the diameter of the airways at generation n. Also there are 2^n airways in generation n according to the Weibel model (Weibel 1963). We also assumed that the liquid plug velocity is the same as the average air velocity at each airway.

We choose $d_0 = 1.7$ cm and $Q = 500$ cm^3 s^{-1}, which are average values for adults. Typical values of mucus properties are: $\tau_y = 400$ dyne cm^{-2}, $\mu_p = 1$ P, $\sigma = 80$ dyne cm^{-1} and $\rho = 1$ g cm^{-3} (Bush *et al.* 2006). Using these dimensional parameter values, Bn is constant for all generations and it is ∼1.5. However, Ca and Re decrease with increasing n. For $n \geqslant 14$, which is the subject of this study, Re is less than 1. Therefore, for the steady motion in those generations, the effects of the fluid inertia can be neglected. At generations 1, 10 and 15, Ca/Re are 2.19/236, 0.27/3.7 and 0.086/0.6, respectively.

Based on the above assumptions, $\mu_p v_{tip}^*/b$, which is the stress and pressure scale in this study, does not vary with n. As a result, the trends of variations of the dimensional and dimensionless stresses and pressure with n are similar.

6. Results and discussion

In this section the results of a parametric study are presented. In most of the examples, L_P is 1, while the effects of the plug length on some of the results are also discussed. The tip of the leading meniscus is always at $x = 0$.

https://doi.org/10.1017/jfm.2011.438 Published online by Cambridge University Press

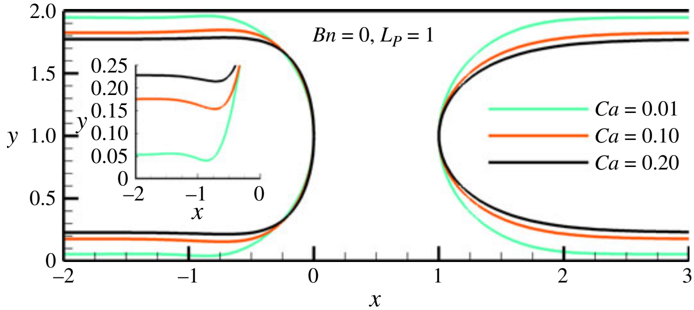

FIGURE 2. (Colour online available at journals.cambridge.org/flm) Variation of the plug shape with Ca for a Newtonian case. The inset shows a close-up from the wavy region of the leading meniscus.

Ca	Current study, $L_p = 1$	Fujioka & Grotberg (2004), $L_P = 2$	Reinelt & Saffman (1985), semi-infinite finger
0.01	0.0540	0.0535 (0.9 %)	0.0540 (0 %)
0.10	0.1750	0.1790 (−2.2 %)	0.1760 (−0.6 %)
0.20	0.2277	0.2340 (−2.7 %)	0.2268 (0.4 %)

TABLE 1. Variation of h with Ca for a Newtonian plug in comparison with some previous computational works.

Figure 2 shows the profile of a liquid plug for $Ca = 0.01$, 0.1 and 0.25, and $Bn = 0$ and $L_P = 1$. For $Ca = 0.01$, the two menisci are nearly symmetric, but capillary waves are present on the transient region of the leading meniscus. The transient sections are followed by two flat regions, liquid films, where the gradients of the velocity components in both x and y directions are nearly zero. The increase in Ca flattens and sharpens the leading and trailing menisci, respectively. The thickness of the liquid film, h, increases and the amplitude of the capillary waves decreases by increasing Ca. Table 1 favourably compares the computed film thickness with some previous computational works for advancing gas fingers and liquid plugs.

The asymmetry in the plug shape under the Stokes flow condition is due to the pressure difference between the two gas phases. The asymmetry in the plug shape leads to the asymmetry in the profile of the wall shear stress, as we will demonstrate later. It should be noted that, even for the Stokes flow condition, the problem is nonlinear owing to the free surface boundary conditions.

Figure 3(*a–c*) show the profile of a liquid plug for different Bn and $Ca = 0.025$, 0.05 and 0.1 with $L_P = 1$. The amplitude of the capillary waves along the leading meniscus decreases with increasing Bn. The effect, however, becomes more profound at larger Ca, as the ratio of the yield stress to the surface tension, $Bn \times Ca$, increases. This behaviour is consistent with the suppression of capillary waves with increasing Ca in Newtonian plugs and bubbles, as demonstrated by Giavedoni & Saita (1999), Fujioka & Grotberg (2004) and Feng (2009). The yield stress is a component of the viscous stress; therefore increasing the yield stress enhances the viscous effects against surface tension. The local interaction between the viscous stress

https://doi.org/10.1017/jfm.2011.438 Published online by Cambridge University Press

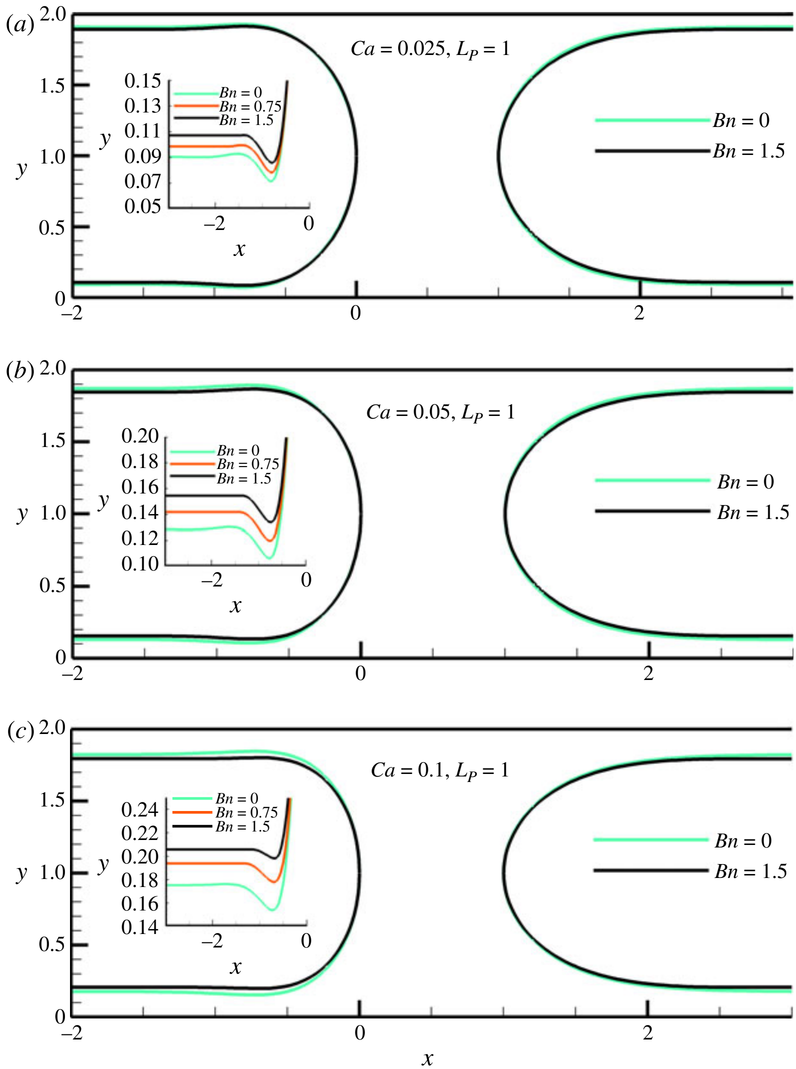

FIGURE 3. (Colour online) Profile of a liquid plug for different Bn and Ca with $L_P = 1$. The insets show close-ups from the wavy region of the leading meniscus.

and the surface tension modifies the local pressure, and as a result the amplitude of the waves decreases.

Figure 4 shows the variation of h with Bn for $Ca = 0.025$, 0.05 and 0.1 with $L_p = 1$. Here h increases with increasing Bn for all Ca values. This is also consistent with increase of h with Ca in Newtonian plugs. For $Ca = 0.1$ a cubic polynomial fits very well ($R^2 = 0.9997$ for a cubic polynomial fit for this case, where R^2 is defined as the ratio of the sum of the squares of the regression and the total sum of the squares) for variation of h with Bn for the range of computed data. For the two other Ca, the variation of h with Bn is nearly linear for the range of provided data. At $Bn = 1.5$, h is $\sim$20 % larger than that for the Newtonian fluid for all three values of Ca.

Figure 5 shows the variation of Δp with Bn for $Ca = 0.025$, 0.05 and 0.1. For the range of parameters studied, the variation of Δp with Bn for all three values of

https://doi.org/10.1017/jfm.2011.438 Published online by Cambridge University Press

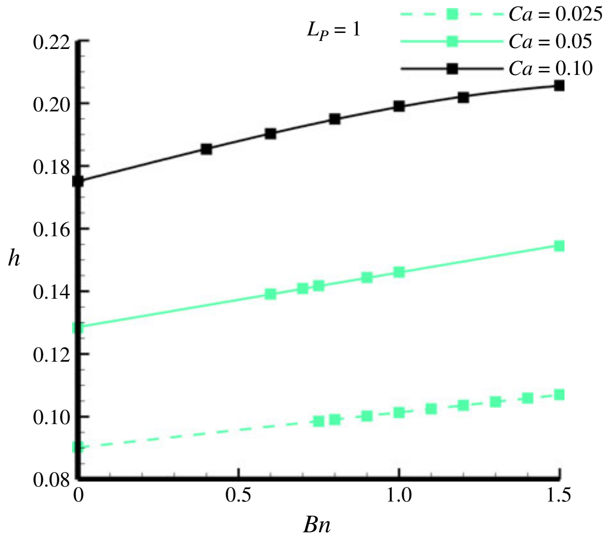

FIGURE 4. (Colour online) Variation of h with Bn and Ca, with $L_P = 1$.

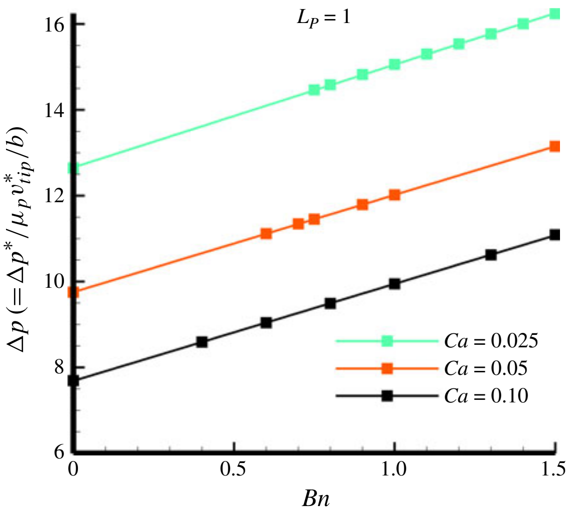

FIGURE 5. (Colour online) *Plot of* Δp for different Bn and Ca, with $L_P = 1$.

Ca is linear. The increase in Δp with Bn is due to the yield stress, which has to be overcome during the motion. At $Bn = 1.5$, Δp increases ~28 %, 35 % and 44 % compared to the Newtonian fluid for $Ca = 0.025$, 0.05 and 0.1, respectively. Owing to the surface tension effect, the dimensional Δp increases for lower generations (larger n) where Ca is smaller.

Figure 6(*a*,*b*) show the velocity vectors, streamlines and contours of V_x for liquid plugs with $Ca = 0.1$, $L_p = 1$ and $Bn = 0$ and 1.5, respectively. Only the areas covering the core flow between the two menisci and the regions around the transient sections of each meniscus were plotted. For the Newtonian fluid, there are two counter-rotating vortices in the core region between the two menisci. For $Bn = 1.5$, however, the

https://doi.org/10.1017/jfm.2011.438 Published online by Cambridge University Press

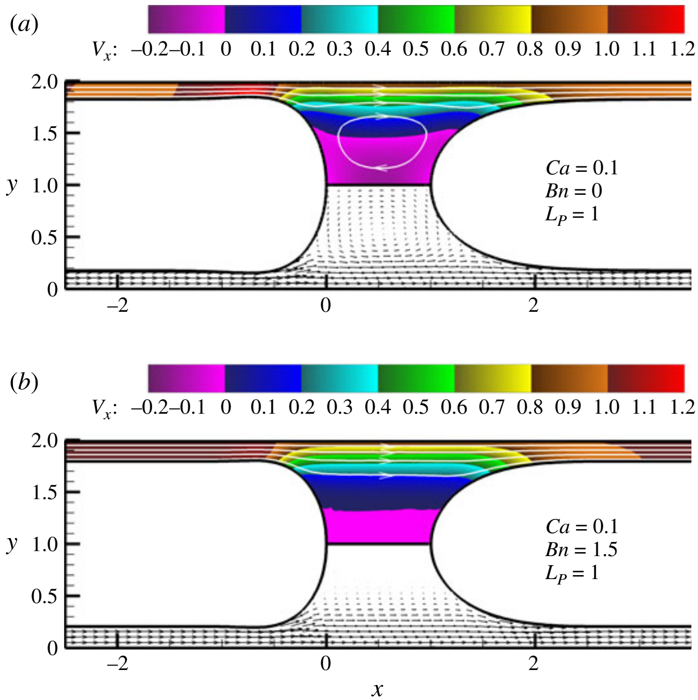

FIGURE 6. (Colour online) Velocity vectors, streamlines and contours of V_x for (*a*) Newtonian and (*b*) Bingham liquid plugs. Bottom half: velocity vectors. Top half: contours of V_x and streamlines.

fluid velocity is nearly zero in this region. This suggests that the region is unyielded. The value of $|dV_x/dx|$ is larger in the region beneath the transient section of the leading meniscus in the Newtonian fluid. This is consistent with the suppression of the capillary waves at the leading meniscus by the yield stress. Contours of V_x and streamlines are more curved in the lower part of the core flow between the two menisci, $0.2 < x < 0.8$ and $0.2 < y < 0.5$ / $1.5 < y < 1.8$ for the Newtonian fluid. This is due to the larger local apparent viscosity of the Bingham fluid compared to the viscosity of the Newtonian fluid. The deviation from the Newtonian patterns is less visible for the two other smaller Ca values, which have not been plotted here. This trend is expected, as $Bn \times Ca$ (which is the ratio of the yield stress to the surface tension) becomes smaller for the other Ca.

Figures 7(*a–c*) and 8(*a–c*) show the profiles of D_{12} and τ_{12} along the wall for different Bn and for $Ca = 0.025$, 0.05 and 0.1 with $L_P = 1$. The value of nearly all maxima of $|D_{12}|$ decreases with increasing Bn. Also, the wavy regions of the profile of D_{12}, which are beneath the front meniscus, $-2 < x < -1.5$ and $0 < x < 2$, become flatter with increasing Bn. These are all due to the larger apparent viscosity of a Bingham fluid compared to a Newtonian one.

The reduction of $|D_{12}|$, however, does not necessarily lead to the decrease in $|\tau_{12}|$. From (3.3) and (3.4) it can be deduced that the wall shear stress in the yielded regions for a large value of m is

$$\tau_{12} \cong D_{12} + Bn, \quad \tau_{12} \geqslant Bn, \tag{6.1a}$$

$$\tau_{12} \cong D_{12} - Bn, \quad \tau_{12} \leqslant -Bn. \tag{6.1b}$$

https://doi.org/10.1017/jfm.2011.438 Published online by Cambridge University Press

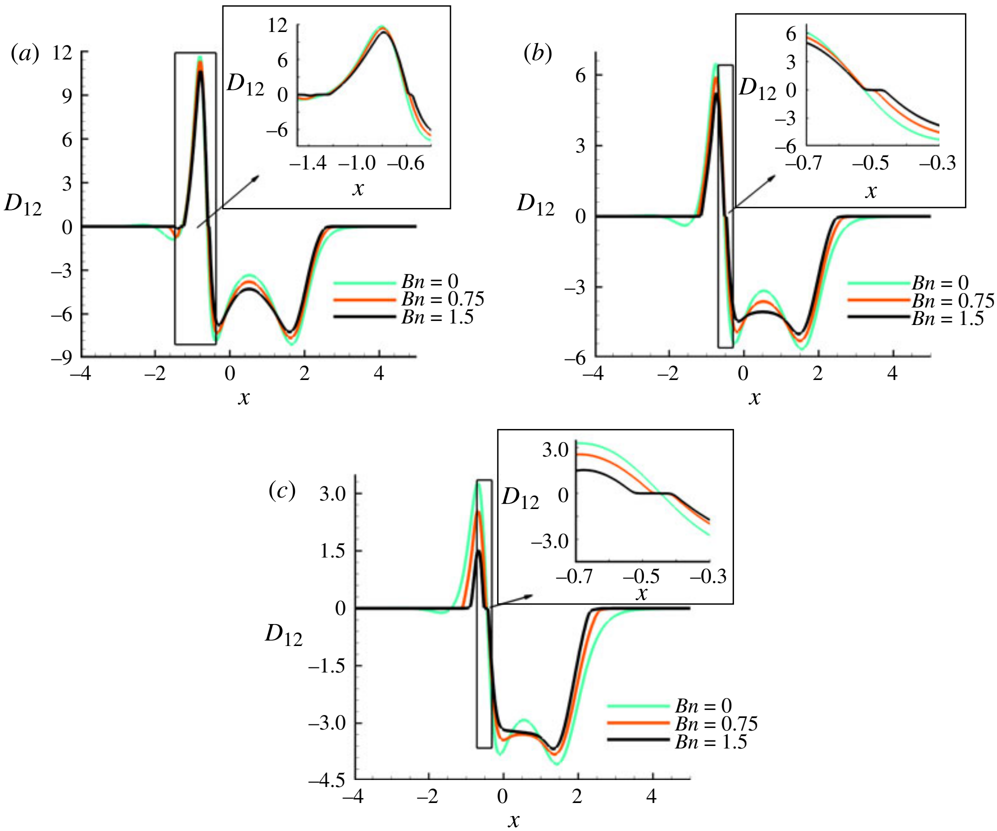

FIGURE 7. (Colour online) Profile of D_{12} along the wall for different *Bn* and *Ca*, with $L_P = 1$: (*a*) $Ca = 0.025$, $L_p = 1$; (*b*) $Ca = 0.05$, $L_p = 1$; (*c*) $Ca = 0.1$, $L_p = 1$. The insets show close-ups of the line segments where D_{12} changes its sign.

At any point in the yielded regions, then, the wall shear stress is the sum of the yield stress, which is *Bn* ($-Bn$ for the negative stresses) non-dimensionally, and the shearing due to D_{12}. This leads to some qualitative differences in the profiles of D_{12} and τ_{12}, where at some points $|D_{12}|$ decreases while $|\tau_{12}|$ increases with increasing *Bn*. The maximum of $|\tau_{12}|$ beneath the leading meniscus remains nearly unchanged with the variation of *Bn* for all three values of *Ca*. The maximum of $|\tau_{12}|$ beneath the trailing meniscus, however, increases with increasing *Bn* and the increase becomes more profound as *Ca* gets larger. For example, at $Ca = 0.1$, for $Bn = 1.5$, $|\tau_{12}|$ is 27 % larger than that for $Bn = 0$. This shows that, beneath the trailing meniscus, the increase in $|\tau_{12}|$ with the yield stress dominates over its decrease with the shearing.

For all computed values of *Bn*, the global maximum of $|\tau_{12}|$ for $Ca = 0.025$ and 0.05 is at some points beneath the leading meniscus, while for $Ca = 0.1$ it is beneath the trailing one. The increase in *Bn* leads to an increase in the maximum of $|\tau_{12}|$ beneath the trailing meniscus, though it does not significantly alter the value of the maximum beneath the leading meniscus, so the global maximum of $|\tau_{12}|$ may shift from the front to the back in some cases solely due to the yield stress. Figure 8(*d*) shows that for the Newtonian fluid with $Ca = 0.06$, the global maximum of $|\tau_{12}|$ is at a point beneath the leading meniscus where $x = -0.73$, while for the same *Ca*

https://doi.org/10.1017/jfm.2011.438 Published online by Cambridge University Press

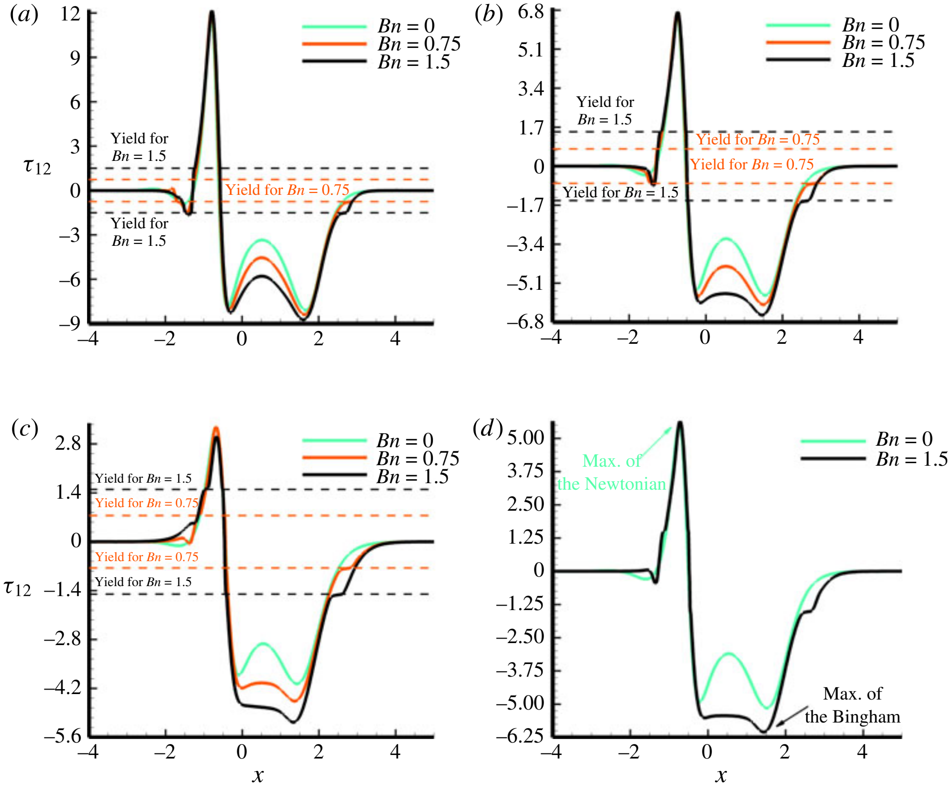

FIGURE 8. (Colour online) Profile of τ_{12} along the wall for different Bn and Ca, with $L_P = 1$: (*a*) $Ca = 0.025$, $L_p = 1$; (*b*) $Ca = 0.05$, $L_p = 1$; (*c*) $Ca = 0.1$, $L_p = 1$; (*d*) $Ca = 0.06$, $L_p = 1$.

and $Bn = 1.5$, the global maximum occurs at a point beneath the trailing meniscus where $x = 1.44$.

The insets in figure 7(*a–c*) show the close-ups of the regions where D_{12} changes its sign at the wall. While for the Newtonian fluid, D_{12} changes its sign as it passes through a single point with $D_{12} = 0$, the stagnation point, the change in sign of D_{12} for the Bingham fluid occurs at the two sides of a line segment where D_{12} is almost zero, e.g. $-0.52 \leqslant x \leqslant -0.42$ in figure 7(*c*) for $Ca = 0.1$ and $Bn = 1.5$. The line segment in fact is an unyielded region according to the yield criteria for the regularized method. The length of the segment increases with increasing Bn or Ca. Therefore, in Bingham fluids (approximated by a regularized method), instead of a single stagnation point beneath the leading meniscus on the wall, there is an unyielded line segment.

Another important quantity regarding epithelial cell injuries is $|\mathrm{d}\tau_{12}/\mathrm{d}x|$ (Bilek, Dee & Gaver 2003). Increase in $|\mathrm{d}\tau_{12}/\mathrm{d}x|$ caused by any mechanism can be a major contributor to injuries of the epithelial cells.

Figure 9(*a–c*) show close-ups of τ_{12} at the unyielded line segments. It is inferred that $|\mathrm{d}\tau_{12}/\mathrm{d}x|$ increases significantly in those line segments (where $|\mathrm{d}D_{12}/\mathrm{d}x|$ is almost zero) compared to the neighbouring areas and the rest of the wall. The increase of $|\mathrm{d}\tau_{12}/\mathrm{d}x|$ in those segments is not because of an increase in $|\mathrm{d}D_{12}/\mathrm{d}x|$ but is due to the sharp variation of τ_{12} across the segments. The profile of τ_{12} in the core of the unyielded line segments looks to be linear, varying from Bn to $-Bn$ despite

https://doi.org/10.1017/jfm.2011.438 Published online by Cambridge University Press

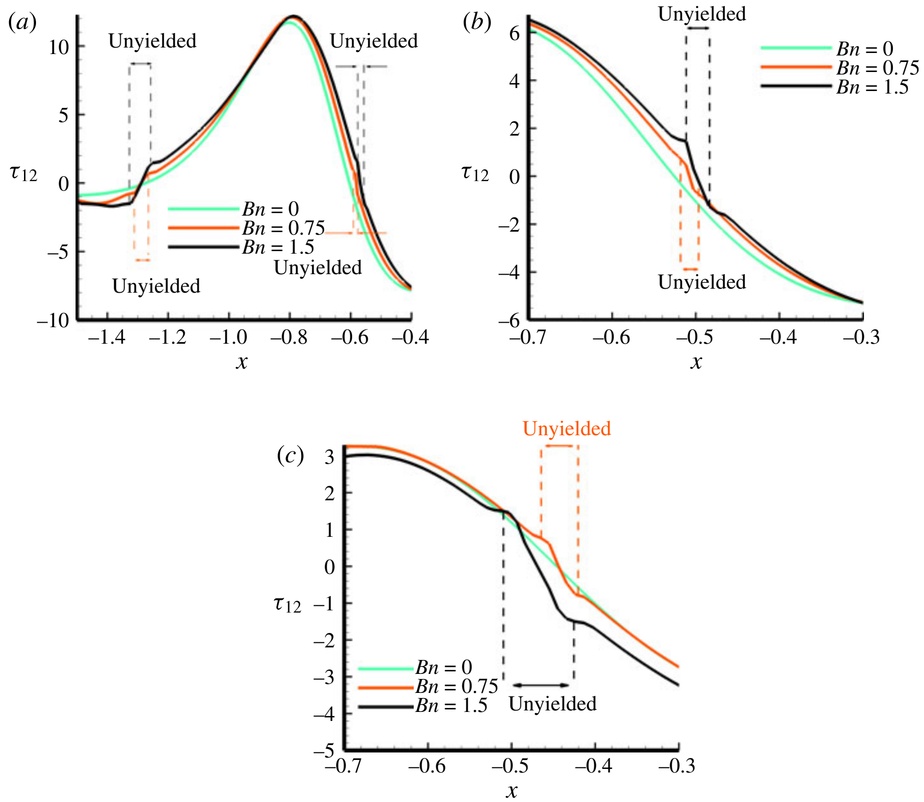

FIGURE 9. (Colour online) Profile of τ_{12} along the unyielded line segment where D_{12} changes its sign: (*a*) $Ca = 0.025$, $L_p = 1$; (*b*) $Ca = 0.05$, $L_p = 1$; (*c*) $Ca = 0.1$, $L_p = 1$.

the low-amplitude oscillations due to the sharp gradient of the apparent viscosity. Therefore the value of $|d\tau_{12}/dx|$ in the unyielded segments can be approximated by $2Bn/L_{us}$, where L_{us} is the length of the unyielded segment. The value of L_{us} increases with increase in Bn or Ca, as shown in figures 7(*a–c*) and 9(*a–c*). Therefore, the maximum of $|d\tau_{12}/dx|$ increases with decreasing Ca. This indicates that the airway walls at the lower generations (larger n, smaller Ca) experience greater gradients of the shear stress. The trend of variation of $|d\tau_{12}dx|$ with Bn, however, cannot be speculated without computation. We need to emphasize that in general L_{us} depends on m as it decreases with increasing m. This would enhance the aforementioned effects of Bn and Ca on the maximum of $|d\tau_{12}/dx|$ along the wall.

As Bilek *et al.* (2003) and Kay *et al.* (2004) explain, $|dp/dx|$ along the wall is another quantity significantly affecting epithelial cell injuries in the respiratory airways. Figure 10(*a*) shows the profile of p along the wall for $Ca = 0.1$ and different Bn with $L_P = 1$. The profile of p varies dramatically beneath the leading and trailing transitions owing to the surface tension and geometry effects. Beneath the films, where the shear stress is small, the profile of p is flat. For each Bn value, examination of the data reveals that the global maximum of $|dp/dx|$ again is at a point inside the unyielded line segment beneath the leading meniscus. For $Ca = 0.1$, the magnitude of the global maximum increases ∼15 % at $Bn = 1.5$ compared to that for the Newtonian fluid. Figure 10(*b*) shows the profile of p along the wall

https://doi.org/10.1017/jfm.2011.438 Published online by Cambridge University Press

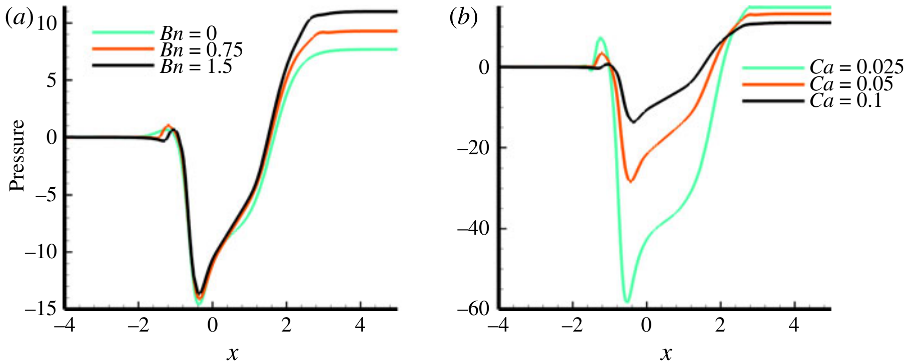

FIGURE 10. (Colour online) Profile of p along the wall for $L_P = 1$: (*a*) variation with Bn, for $Ca = 0.1$; (*b*) variation with Ca, for $Bn = 1.5$.

for $Bn = 1.5$ and different Ca with $L_P = 1$. Examination of the data shows that the global maximum of $|\mathrm{d}p/\mathrm{d}x|$ increases significantly with decreasing Ca owing to surface tension effects. Examination of the data shows that, for $Bn = 0$ and 1.5, the global maximum increases by a factor of 5 and 4.5, respectively, when Ca decreases from 0.1 to 0.025. This indicates that the airways at the lower generations (larger n) experience larger dimensional pressure gradients.

We again emphasize that the maximum values of $|\mathrm{d}\tau_{12}/\mathrm{d}x|$ and $|\mathrm{d}p/\mathrm{d}x|$ in general depend on m. Therefore, the trend of the variation of $|\mathrm{d}\tau_{12}/\mathrm{d}x|$ and $|\mathrm{d}p/\mathrm{d}x|$ with Bn and Ca should be looked at in a qualitative way. For one of the computed cases, however, we will show that the profile of the wall shear stress converges with m.

Figure 11(*a–d*) show the contour of $\dot{\gamma}$ and $|\tau|$ for $Ca = 0.1$, $L_P = 1$ and different Bn. The top and bottom halves in each figure are contours of $\dot{\gamma}$ and $|\tau|$, respectively. The unyielded regions are in white. The unyielded regions grow in the adjacent wall film with increasing Bn. The unyielded area also appears and grows in the core region between the two menisci. At $Bn = 1.5$, the middle of the core, $0 < x < 1$ and $0.6 < y < 1.4$, is entirely unyielded, which is consistent with the velocity vectors in figure 6(*b*). This is also in qualitative agreement with the computational results by Thompson *et al.* (2010) for an axisymmetric advancing gas finger, where an infinite unyielded strip is attached to the front tip for large enough dimensionless yield stress. The stress level in the region adjacent to the wall between $-0.2 < x < 2$ increases with increasing Bn. This is consistent with the increase in Δp with Bn. The global maxima of $\dot{\gamma}$ and $|\tau|$ decrease and increase with increasing Bn, respectively, which indicates that the yield stress reduces the maximum of the shearing but enhances the maximum of the von Mises stress. For all four cases, the von Mises stress attains its maximum value near the interface of the leading meniscus in the transition region. This differs significantly from the situation in fully developed two-dimensional Bingham channel flows, where the maximum of the von Mises stress is always at the wall.

Figure 12(*a–c*) show the contours of $|\tau|$ for $Bn = 0.6$, $Ca = 0.1$ and different L_P. With decreasing L_P, the unyielded areas grow in the core region between the two menisci. As an example, when $L_P = 0.25$, the middle of the core, $0.6 < y < 1.4$, is entirely unyielded. This is expected, as the two tips are stationary and therefore the reduction in the plug length leads to a lower level of local shearing. The value of Δp increases with increasing L_P since a longer portion of the wall is being exposed to the induced shear stress by the fluid. Examination of the data shows that, for this set of Bn

https://doi.org/10.1017/jfm.2011.438 Published online by Cambridge University Press

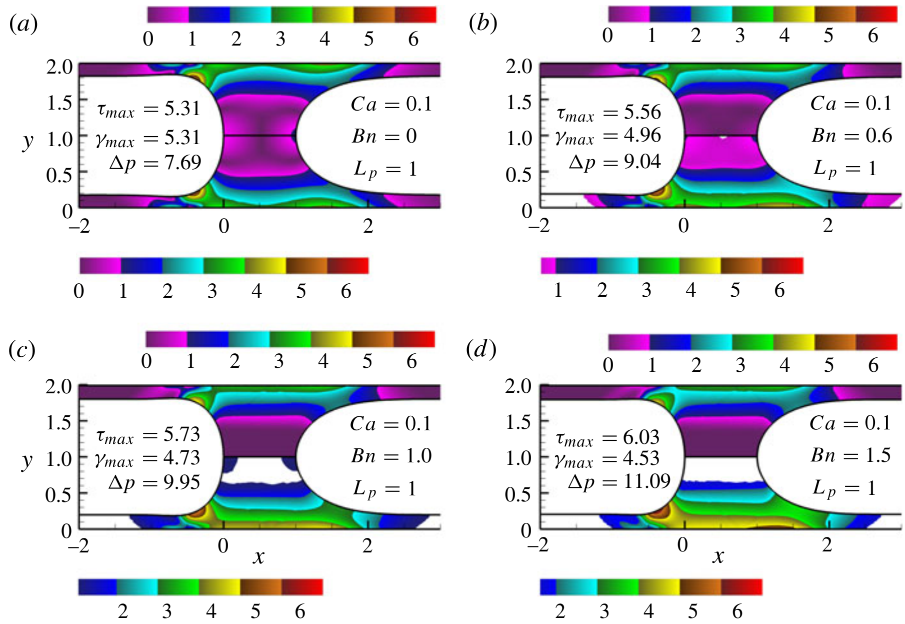

FIGURE 11. (Colour online) Contours of $\dot{\gamma}$ and $|\tau|$ for $Ca = 0.1$ and different Bn, with $L_P = 1$. The top and bottom halves show the contours of $\dot{\gamma}$ and $|\tau|$, respectively.

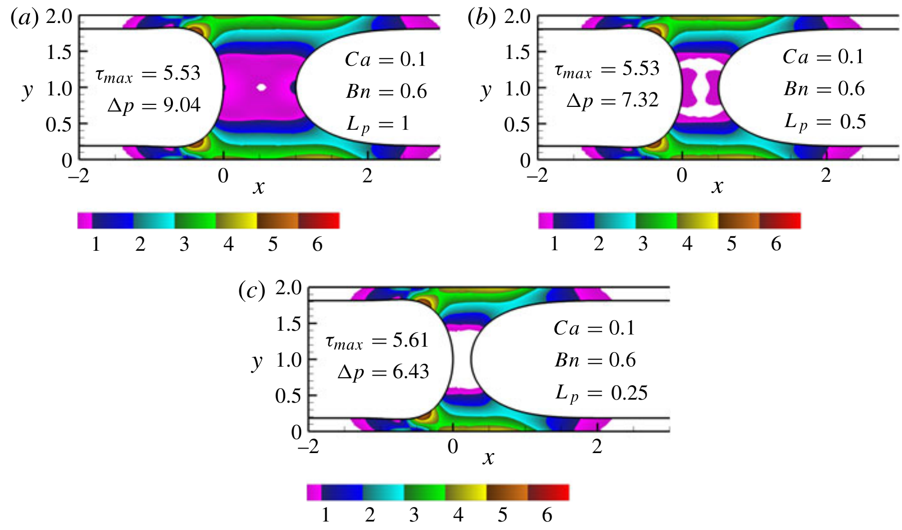

FIGURE 12. (Colour online) Contours of $|\tau|$ for $Ca = 0.1$ and $Bn = 0.6$, with different L_P.

and Ca, the variation of Δp with L_P is linear. The computed results also show that the film thickness decreases by 2.6 % and the global maximum of $|\tau_{12}|$ along the wall increases by 3.5 % when L_P decreases from 1 to 0.25. Therefore, for this set of Bn and Ca, the plug length mainly alters the topology of the yield surfaces.

We performed all the presented computations with $m = 1000$. In order to investigate the effects of the value of m on the results, we repeated the simulations for $Ca = 0.1$,

https://doi.org/10.1017/jfm.2011.438 Published online by Cambridge University Press

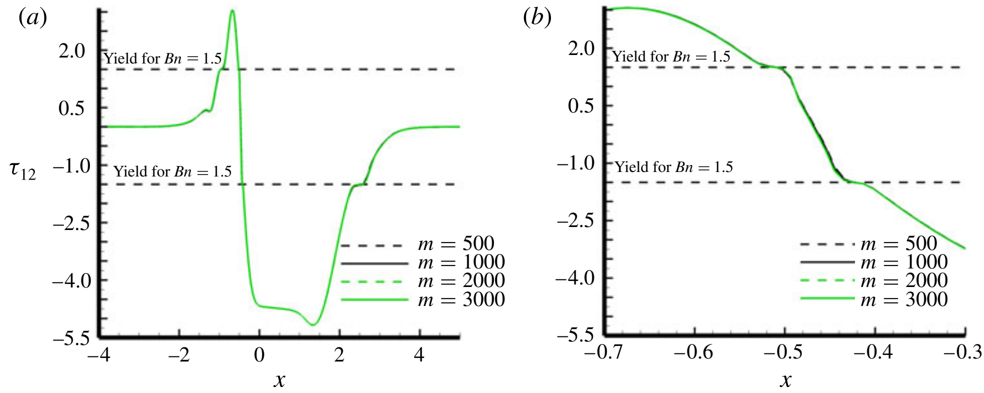

FIGURE 13. (Colour online) Wall shear stress for different values of m, with $Ca = 0.1$, $Bn = 1.5$ and $L_P = 1$: (*a*) entire wall; (*b*) close-up of the unyielded line segment where D_{12} changes sign.

$Bn = 1.5$ and $L_P = 1$ with three different values of m ranging from 500 to 3000. We examined the plug shape and the location of the yield surfaces for different values of m for this case. The plug shape almost did not change with m. On the other hand, the yielded regions grew slightly as m increased. The growth rate, however, became slower as m increased. This suggests that the location of the yield surfaces converges with m for this case.

Figure 13(*a*) shows the wall shear stress for $Ca = 0.1$, $Bn = 1.5$ and $L_P = 1$ and four different values of m ranging from 500 to 3000. The profile of the wall shear stress is almost the same for all values of m. Figure 13(*b*) shows a close-up of the wall shear stress for the same cases along the unyielded line segment where D_{12} changes its sign and $|d\tau_{12}/dx|$ attains its maximum. The wall shear stress profiles are nearly the same in this region as well. As a general trend, the unyielded regions shrink as the value of m increases. This is also true for the unyielded line segment where D_{12} changes its sign and $|d\tau_{12}/dx|$ attains its maximum. As a result, the maximum of $|d\tau_{12}/dx|$ from the Bingham fluid equation would be greater than that computed from regularized methods with finite values for m. This confirms even further one of our findings in this work that the maximum of $|d\tau_{12}/dx|$ along the wall is larger for Bingham fluids compared to Newtonian ones.

Figure 14(*a*) shows the dimensionless driving pressure $\Delta\pi_p = (p_1^* - p_2^*)/(\sigma/b)$ for a Newtonian and a Bingham liquid plug with $L_P = 1$ propagating with different speeds in a two-dimensional channel with fixed dimensions. The data points (as we examined, the driving pressure and h are nearly insensitive to m, and therefore we used $300 < m < 500$ for $Ca < 0.025$ to ease the numerical convergence) are individual computational results and the dashed curve segments are best-fitting polynomial extrapolations of cubic order. Under these conditions, $Bn \times Ca = \tau_y b/\sigma$ is zero for the Newtonian fluid and 0.04 for the Bingham fluid. Then Ca will be the only dimensionless parameter that depends on plug velocity. The driving pressure decreases with decreasing Ca owing to the decrease of wall shear stress. The driving pressure for the Bingham fluid is always greater than the Newtonian one owing to the yield stress. The driving pressure difference in the limit of $Ca \to 0$, $\Delta\pi_{p0}$, is zero for the Newtonian fluid but it is non-zero for the Bingham one owing to the yield stress. The extrapolated value for the Bingham fluid is $\Delta\pi_{p0} \sim 0.182$, but the extrapolated value

https://doi.org/10.1017/jfm.2011.438 Published online by Cambridge University Press

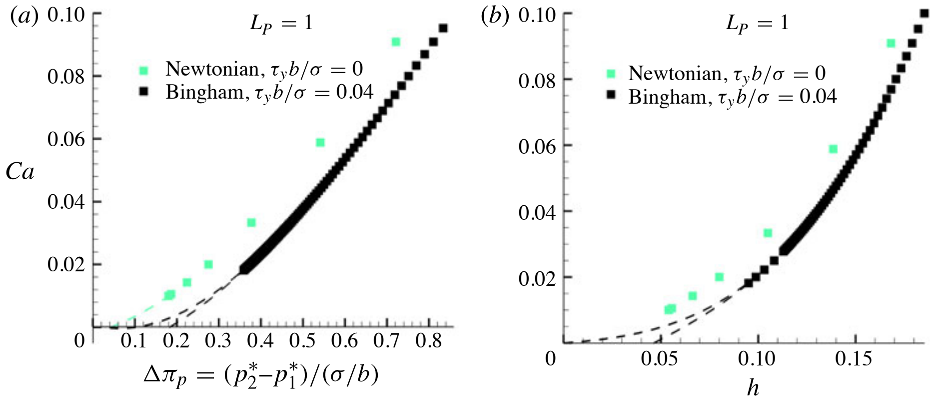

FIGURE 14. (Colour online) (*a*) Driving pressure difference and (*b*) film thickness for a Newtonian and a Bingham plug, propagating with different speeds in a channel with fixed dimensions, with $L_P = 1$.

for the Newtonian fluid is $\Delta\pi_{p0} \sim 0.04$ rather than $\Delta\pi_{p0} = 0$. So there is some room left for improvement through adding more data points for lower Ca values. It should be mentioned that, as Ca gets smaller, Bn gets larger, and this combination inevitably creates issues for the computational convergence after some point. For most of the Ca range, the difference between Newtonian and Bingham $\Delta\pi_p$ is roughly 0.1, which dimensionally is 2.5 times the yield stress. For two-dimensional flow in a channel filled with a Bingham fluid, it can be shown that the dimensional pressure drop for unit axial length is τ_y/b for the motion to be initiated. Therefore, for a segment of the channel with length equal to the half-width of the channel, the driving pressure for the initiation of the motion, $\Delta\pi_{c0}$, becomes $\tau_y/\sigma/b$, which is 0.04 for this case. We consider this value as a lower bound for $\Delta\pi_{p0}$, as $\Delta\pi_p > \Delta\pi_c$ for the same channel flow centreline velocity as the plug speed. Using this value, we provided another dashed curve segment in figure 14(*a*) as a lower bound for $\Delta\pi_p$ in the region where there are no computational data. Hence, we can suggest that $\Delta\pi_p$ in this region is bounded between the two dashed curves.

Figure 14(*b*) shows h for the Newtonian and Bingham fluids in terms of the Ca values for the same case. Again, the data points are the individual computational data and the dashed lines are extrapolations. For both the Bingham and Newtonian fluids, h decreases with decreasing Ca. It is bigger for the Bingham compared to the Newtonian for the range of computed data. The thickness must asymptote to zero for the Newtonian fluid. For the Bingham fluid in the region where there are no computational data, the value of h lies between the two extrapolated dashed lines where one passes through the origin.

7. Conclusions

The steady motion of Bingham liquid plugs in two-dimensional channels was studied numerically through using a regularized constitutive equation. The governing equations were discretized by a mixed finite element formulation and the free surfaces were resolved by the method of spines.

From our numerical results, the following conclusions are drawn. The thickness of the static film increases with increasing Bn. Also, the amplitude of the capillary waves at the leading meniscus decreases with the increase in Bn. The wall stresses and their

https://doi.org/10.1017/jfm.2011.438 Published online by Cambridge University Press

gradients all are magnified by the increase in Bn. The effect is more profound on $|d\tau_{12}/dx|$ and it is followed by $|\tau_{12}|$ and $|dp/dx|$, respectively. Therefore, the motion of mucus plugs can be much more damaging to the airway epithelial cells, specifically due to significant enhancement of $|d\tau_{12}/dx|$ by the yield stress. (We should note that, for the airway epithelial cells, the damage might be less severe since the cells are in contact with a serous layer.) The driving pressure difference increases with Bn linearly for all the computed values of Ca. The unyielded area grows in the core region between the two menisci and also in the adjacent wall film with the increase in Bn. The plug length mostly affects the topology of the yield surfaces in the core region between the two menisci. In all the computed cases, the maximum of the von Mises stress occurred in the transition region of the leading meniscus, while for a channel flow the maximum always occurs at the wall. The computational results also suggest that, for Bingham plugs that move very slowly, $Ca \to 0$, the driving pressure is non-zero.

Acknowledgements

The authors would like to thank NIH for supporting this work through the grants HL84370 and HL85156. Thanks also are given to M. M. Denn (Levich Institute of CUNY), H. Fujioka (Tulane University), D. Halpern (University of Alabama, Tuscaloosa) and J. Kulkarani (ANSYS Inc.) for informative discussions.

REFERENCES

ALLOUCHE, M., FRIGAARD, I. A. & SONA, G. 2000 Static wall layers in the displacement of two visco-plastic fluids in a plane channel. *J. Fluid Mech.* **424**, 243–277.

ANSYS FIDAP, 2003 *User's Manual*. ANSYS Inc., Version 8.7.

BEAULNE, M. & MITSOULIS, E. 1997 Creeping motion of a sphere in tubes filled with Herschel–Bulkley fluids. *J. Non-Newtonian Fluid Mech.* **72** (1), 55–71.

BIAN, S., TAI, C. F., HALPERN, D., ZHENG, Y. & GROTBERG, J. B. 2010 Experimental study of flow fields in an airway closure model. *J. Fluid Mech.* **647**, 391–402.

BILEK, A. M., DEE, K. C. & GAVER, D. P. 2003 Mechanisms of surface-tension-induced epithelial cell damage in a model of pulmonary airway reopening. *J. Appl. Physiol.* **94** (2), 770–783.

BURGER, E. J. & MACKLEM, P. 1968 Airway closure – demonstration by breathing 100 percent O_2 at low lung volumes and by N_2 washout. *J. Appl. Physiol.* **25** (2), 139.

BURGOS, G. R., ALEXANDROU, A. N. & ENTOV, V. 1999 On the determination of yield surfaces in Herschel–Bulkley fluids. *J. Rheol.* **43** (3), 463–483.

BUSH, A., PAYNE, D., PIKE, S., JENKINS, G., HENKE, M. O. & RUBIN, B. K. 2006 Mucus properties in children with primary ciliary dyskinesia – comparison with cystic fibrosis. *Chest* **129** (1), 118–123.

DIMAKOPOULOS, Y. & TSAMOPOULOS, J. 2003 Transient displacement of a viscoplastic material by air in straight and suddenly constricted tubes. *J. Non-Newtonian Fluid Mech.* **112** (1), 43–75.

DIMAKOPOULOS, Y. & TSAMOPOULOS, J. 2007 Transient displacement of Newtonian and viscoplastic liquids by air in complex tubes. *J. Non-Newtonian Fluid Mech.* **142** (1–3), 162–182.

DUBASH, N. & FRIGAARD, I. 2004 Conditions for static bubbles in viscoplastic fluids. *Phys. Fluids* **16** (12), 4319–4330.

ESPINOSA, F. F. & KAMM, R. D. 1999 Bolus dispersal through the lungs in surfactant replacement therapy. *J. Appl. Physiol.* **86** (1), 391–410.

EVERETT, D. H. & HAYNES, J. M. 1972 Model studies of capillary condensation. 1. Cylindrical pore model with zero contact angle. *J. Colloid Interface Sci.* **38** (1), 125.

FENG, J. Q. 2009 A long gas bubble moving in a tube with flowing liquid. *Intl J. Multiphase Flow* **35** (8), 738–746.

https://doi.org/10.1017/jfm.2011.438 Published online by Cambridge University Press

Fujioka, H. & Grotberg, J. B. 2004 Steady propagation of a liquid plug in a two-dimensional channel. *Trans. ASME: J. Biomech. Engng* **126** (5), 567–577.

Fujioka, H. & Grotberg, J. B. 2005 The steady propagation of a surfactant-laden liquid plug in a two-dimensional channel. *Phys. Fluids* **17** (8), 17.

Fujioka, H., Takayama, S. & Grotberg, J. B. 2008 Unsteady propagation of a liquid plug in a liquid-lined straight tube. *Phys. Fluids* **20** (6), 13.

Fung, Y. C. 1984 *Biomechanics*. Springer.

Giavedoni, M. D. & Saita, F. A. 1999 The rear meniscus of a long bubble steadily displacing a Newtonian liquid in a capillary tube. *Phys. Fluids* **11** (4), 786–794.

Glowinski, R. 1984 *Numerical Methods for Nonlinear Variational Problems*. Springer.

Glowinski, R., Lions, J. L. & Tremolieres, R. 1981 *Numerical Analysis of Variational Inequalities*. North-Holland.

Halpern, D. & Grotberg, J. B. 1992 Fluid-elastic instabilities of liquid-lined flexible tubes. *J. Fluid Mech.* **244**, 615–632.

Halpern, D., Jensen, O. E. & Grotberg, J. B. 1998 A theoretical study of surfactant and liquid delivery into the lung. *J. Appl. Physiol.* **85** (1), 333–352.

Heil, M. 1999*a* Minimal liquid bridges in non-axisymmetrically buckled elastic tubes. *J. Fluid Mech.* **380**, 309–337.

Heil, M. 1999*b* Airway closure: occluding liquid bridges in strongly buckled elastic tubes. *Trans. ASME: J. Biomech. Engng* **121** (5), 487–493.

Howell, P. D., Waters, S. L. & Grotberg, J. B. 2000 The propagation of a liquid bolus along a liquid-lined flexible tube. *J. Fluid Mech.* **406**, 309–335.

Huh, D., Fujioka, H., Tung, Y. C., Futai, N., Paine, R., Grotberg, J. B. & Takayama, S. 2007 Acoustically detectable cellular-level lung injury induced by fluid mechanical stresses in microfluidic airway systems. *Proc. Natl Acad. Sci. USA* **104** (48), 18 886–18 891.

Kamm, R. D. & Schroter, R. C. 1989 Is airway-closure caused by a liquid-film instability? *Respir. Physiol.* **75** (2), 141–156.

Kay, S. S., Bilek, A. M., Dee, K. C. & Gaver, D. P. 2004 Pressure gradient, not exposure duration, determines the extent of epithelial cell damage in a model of pulmonary airway reopening. *J. Appl. Physiol.* **97** (1), 269–276.

Kistler, S. F. & Scriven, L. E. 1984 Coating flow theory by finite-element and asymptotic analysis of the Navier–Stokes system. *Intl J. Numer. Meth. Fluids* **4** (3), 207–229.

Lavrenteva, O. M., Holenberg, Y. & Nir, A. 2009 Motion of viscous drops in tubes filled with yield stress fluid. *Chem. Engng Sci.* **64** (22), 4772–4786.

Liu, B. T., Muller, S. J. & Denn, M. M. 2002 Convergence of a regularization method for creeping flow of a Bingham material about a rigid sphere. *J. Non-Newtonian Fluid Mech.* **102** (2), 179–191.

Long, W., Thompson, T., Sundell, H., Schumacher, R., Volberg, F. & Guthrie, R. 1991 Effects of 2 rescue doses of a synthetic surfactant on mortality-rate and survival without bronchopulmonary dysplasia in 700-gram to 1350-gram infants with respiratory-distress syndrome. *J. Pediatrics* **118** (4), 595–605.

Moyers-Gonzalez, M. A. & Frigaard, I. A. 2004 Numerical solution of duct flows of multiple visco-plastic fluids. *J. Non-Newtonian Fluid Mech.* **122** (1–3), 227–241.

Oldroyd, J. G. 1947*a* A rational formulation of the equations of plastic flow for a Bingham solid. *Proc. Camb. Phil. Soc.* **43** (1), 100–105.

Oldroyd, J. G. 1947*b* Two-dimensional plastic flow of a Bingham solid – A. Plastic boundary-layer theory for slow motion. *Proc. Camb. Phil. Soc.* **43** (3), 383–395.

Papanastasiou, T. C. 1987 Flows of materials with yield. *J. Rheol.* **31** (5), 385–404.

Potapov, A., Spivak, R., Lavrenteva, O. M. & Nir, A. 2006 Motion and deformation of drops in Bingham fluid. *Ind. Engng Chem. Res.* **45** (21), 6985–6995.

Reinelt, D. A. & Saffman, P. G. 1985 The penetration of a finger into a viscous-fluid in a channel and tube. *SIAM J. Sci. Stat. Comput.* **6** (3), 542–561.

Shao, N., Gavriilidis, A. & Angeli, P. 2009 Flow regimes for adiabatic gas–liquid flow in microchannels. *Chem. Engng Sci.* **64** (11), 2749–2761.

https://doi.org/10.1017/jfm.2011.438 Published online by Cambridge University Press

SINGH, J. P. & DENN, M. M. 2008 Interacting two-dimensional bubbles and droplets in a yield-stress fluid. *Phys. Fluids* **20** (4), 11.

DE SOUSA, D. A., SOARES, E. J., DE QUEIROZ, R. S. & THOMPSON, R. L. 2007 Numerical investigation on gas-displacement of a shear-thinning liquid and a visco-plastic material in capillary tubes. *J. Non-Newtonian Fluid Mech.* **144** (2–3), 149–159.

TAI, C. F., BIAN, S., HALPERN, D., ZHENG, Y., FILOCHE, M. & GROTBERG, J. B. 2011 Numerical study of flow fields in an airway closure model. *J. Fluid Mech.* **677**, 483–502.

TAVANA, H., ZAMANKHAN, P., CHRISTENSEN, P. J., GROTBERG, J. B. & TAKAYAMA, S. 2011 Epithelium damage and protection during reopening of occluded airways in a physiologic microfluidic pulmonary airway model. *Biomed. Microdevices* **13**, 731–742.

THOMPSON, R. L., SOARES, E. J. & BACCHI, R. D. A. 2010 Further remarks on numerical investigation on gas displacement of a shear-thinning liquid and a visco-plastic material in capillary tubes. *J. Non-Newtonian Fluid Mech.* **165** (7–8), 448–452.

TSAMOPOULOS, J., DIMAKOPOULOS, Y., CHATZIDAI, N., KARAPETSAS, G. & PAVLIDIS, M. 2008 Steady bubble rise and deformation in Newtonian and viscoplastic fluids and conditions for bubble entrapment. *J. Fluid Mech.* **601**, 123–164.

VOLA, D., BABIK, F. & LATCHE, J. C. 2004 On a numerical strategy to compute gravity currents of non-Newtonian fluids. *J. Comput. Phys.* **201** (2), 397–420.

VOLA, D., BOSCARDIN, L. & LATCHE, J. C. 2003 Laminar unsteady flows of Bingham fluids: a numerical strategy and some benchmark results. *J. Comput. Phys.* **187** (2), 441–456.

WATERS, S. L. & GROTBERG, J. B. 2002 The propagation of a surfactant laden liquid plug in a capillary tube. *Phys. Fluids* **14** (2), 471–480.

WEIBEL, E. R. 1963 *Morphometry of the Human Lung*. Academic Press.

ZHANG, J. Y. 2011 An augmented Lagrangian approach to Bingham fluid flows in a lid-driven square cavity with piecewise linear equal-order finite elements. *Comput. Meth. Appl. Mech. Engng* **199** (45–48), 3051–3057.

ZHENG, Y., FUJIOKA, H., BIAN, S., TORISAWA, Y., HUH, D., TAKAYAMA, S. & GROTBERG, J. B. 2009 Liquid plug propagation in flexible microchannels: a small airway model. *Phys. Fluids* **21** (7), 12.

ZHENG, Y., FUJIOKA, H. & GROTBERG, J. B. 2007 Effects of gravity, inertia, and surfactant on steady plug propagation in a two-dimensional channel. *Phys. Fluids* **19** (8), 16.

https://doi.org/10.1017/jfm.2011.438 Published online by Cambridge University Press